



Time-averaged three-dimensional flow topology in the wake of a simplified car model using volumetric PIV

Prabu Sellappan¹ · Jonathan McNally¹ · Farrukh S. Alvi¹

Received: 30 March 2018 / Revised: 22 May 2018 / Accepted: 27 June 2018 / Published online: 6 July 2018
© Springer-Verlag GmbH Germany, part of Springer Nature 2018

Abstract

Fuel shortages and air pollution are two major incentives for improving the aerodynamics of vehicles. Reducing wake-induced aerodynamic drag, which is strongly dependent on flow topology, is important for improving fuel consumption rates which directly affect the environment. Therefore, a comprehensive understanding of the baseline flow topology is required to develop targeted drag reduction strategies. In this research, the near wake of a generic ground vehicle, a 25° slant Ahmed model at a flow Reynolds number of $Re = 1.1 \times 10^6$, is investigated and its flow topology elucidated. The flow field of this canonical bluff body is extremely rich, with complex flow features such as spanwise trailing wake and streamwise *C*-pillar vortices. The flow is characterized through stereoscopic and tomographic velocity field measurements. The large-scale, horseshoe vortex structures in the trailing wake, conventionally denoted as *A*- and *B*-vortices, are found to vary in size and shape along the spanwise direction, which in turn influence the pressure distribution on the rear vertical surface. The longitudinal *C*-pillar vortices are found to extend far downstream and also influence the trailing wake structures through a complex, three-dimensional interaction. The accuracy and cost of obtaining volumetric information in this complex flow field, by means of volume reconstruction, through Stacked Stereoscopic-Particle Image Velocimetry (PIV) and Tomographic PIV are also investigated.

1 Introduction and background

The aerodynamics of modern day vehicles have been an important research topic due to their impact on fuel efficiency which directly relates to pressing environmental concerns (Kourta and Gillieron 2009). The flow field over a vehicle influences drag and lift forces, both of which are essential to automobile performance. The use of passive flow control (Pujals et al. 2010; Froling and Juechter 2005; Bruneau et al. 2008), which includes changing the shape of the body and adding devices such as spoilers, is used to change these forces according to the performance requirements of a specific car. Balancing the lift force for stability without increasing drag can be a challenge. The drag force, however, is generally desired to be reduced to a minimum.

Automobiles are characterized as bluff bodies, which implies that the pressure drag in the wake of the car is the

greatest contributor to aerodynamic drag, when compared to the friction drag. Ahmed et al. (1984) have shown that the wake of a simplified car model, i.e., Ahmed model, contributes to more than 70% of its drag. Therefore, changing the flow pattern in the wake of an automobile can greatly improve its aerodynamics. Since drag reduction is of interest, in addition to the aforementioned passive methods, a few other passive techniques have been tried. Drag reduction has been successfully implemented through suppression of the 3D separation on the rear slant of the Ahmed model using a rounded edge at the top of the slant (Thacker et al. 2012) and rounded edges along the top and side edges of the slant (Rositto et al. 2016). Many active flow control methods have also been proposed to reduce drag, including a control strategy using steady microjet actuators (Aubrun et al. 2011); drag reduction through the use of fluidic oscillators (Metka and Gregory 2015); active flow control using synthetic jet arrays on Ahmed model with 25° and 35° slants (Park et al. 2013); and Joseph et al. (2012, 2013), who implemented active control through pulsed micro-jets. While these control strategies have been successful to varying degrees, optimal implementation of control devices requires a comprehensive

✉ Prabu Sellappan
psellappan@fsu.edu

¹ Florida Center for Advanced Aero-Propulsion (FCAAP), FAMU-FSU College of Engineering, The Florida State University, 2003 Levy Ave, Tallahassee, FL 32310, USA

understanding of the fully three-dimensional baseline flow topology to effectively target specific flow features.

Although the Ahmed model used in this study has a fairly simple geometry, its wake characteristics have some similarities to the highly complex wake of a modern automobile. While the Ahmed model has a consistent overall shape, its slant angle was originally made interchangeable to observe the effect on flow topology (Ahmed et al. 1984; Corallo et al. 2015). Recently, Tunay et al. (2014) investigated rear slant angles between 25° and 35° and characterized the baseline flow along the wake centerline. The baseline flow for the Ahmed model with 25° and 35° rear slant angles was further characterized in three orthogonal planes by Wang et al. (2013). In the present study, a slant angle of 25° is chosen. This canonical model is utilized to study the rear flow topology without the influence from upstream features unique to each vehicle design, e.g., mirrors and door handles. The use of this simplified model allows for the characterization of the key flow structures present aft of the model.

Various aspects of this canonical flow field have already been studied extensively. Ahmed et al. (1984) identified the key features of the flow and presented a schematic of the vortical structures (see Fig. 1). The unsteady coherent structures, and its concomitant composite spectral content, in the flow field around a 25° Ahmed model at moderate Reynolds numbers ($Re = 0.45 \times 10^5 - 2.4 \times 10^5$) were given by Zhang et al. (2015). Similar information on the unsteady structures and spectral content present on the slant surface along the symmetry plane was given by Thacker et al. (2013). Mean pressure and velocity fields, obtained through an unsteady

simulation based on a lattice Boltzmann approach, have been presented for the symmetry plane and a few selected stream-wise planes by Fares (2006). Extensive velocity profile information obtained using two-component hot-wire and laser Doppler anemometry measurements of the flow upstream and along the symmetry plane of the 25° Ahmed model, helpful for initializing and validating numerical simulations, have been provided in Lienhart et al. (2002) and Lienhart and Becker (2003). The structure of the *A*- and *B*-vortices at a low Reynolds number, $Re \approx 30000$ (based on square root of the frontal area, and an order of magnitude lower than in the present study), and their proposed toroidal nature has been studied by Venning et al. (2017). In addition, there have been a number of studies that have experimentally characterized different aspects of the flow field using planar, two-dimensional, two-component (2D-2C) PIV (McNally et al. 2012; Thacker et al. 2013; Aubrun et al. 2011; Conan et al. 2011). While these studies have provided salient information regarding the baseline flow topology in relevant two-dimensional planes, it is important to bear in mind that the flow around the Ahmed model is inherently three-dimensional and complex. Fully characterizing this flow topology requires obtaining all three components of velocity over a finite volume. This necessitates either quasi-volumetric or volumetric measurements, either through volume reconstruction using multiple two-dimensional, three-component (2D-3C) velocity fields obtained through stereoscopic PIV, or by direct velocity measurements in a volume using tomographic PIV. There are advantages and disadvantages inherent to either approach; the present study explores and characterizes the baseline flow topology using both approaches and also evaluates the performance of the measurement techniques in resolving this complex flow field.

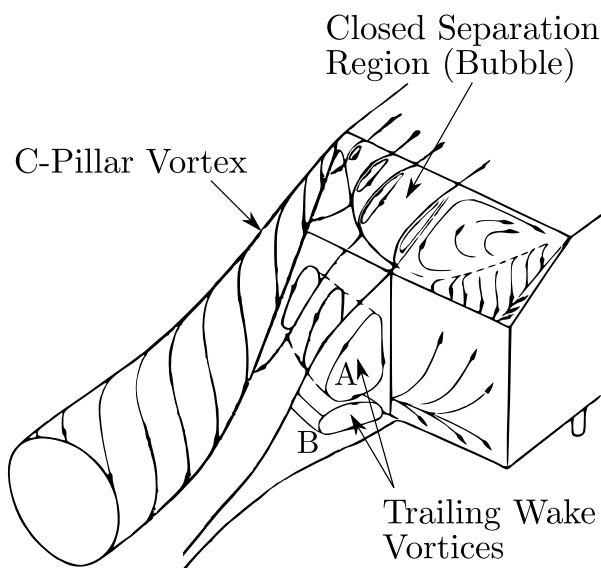


Fig. 1 Schematic of flow structures proposed by Ahmed et al. (1984). Redrawn to improve print quality and is qualitatively similar to the original figure in Ahmed et al. (1984)

2 Experimental details

2.1 Wind tunnel facility description

Experiments were performed in the low-speed wind tunnel located at Florida Center for Advanced Aero-Propulsion (FCAAP) at FAMU-FSU College of Engineering. It is a single-pass, Eiffel-type wind tunnel with test section optical access on all sides. The test section of the wind tunnel has a 0.762 m × 0.762 m cross section with a full length of 1.524 m. For the experiments, a 0.762 m wide by 1.524 m long ground plane with an elliptical leading edge is installed in the facility approximately 0.102 m above the floor to control the size of the incoming boundary layer. The trailing edge of the ground plane is outfitted with an adjustable flap to allow for a nearly constant pressure gradient through the length of the test section. A side view of the model and ground plane is shown in Fig. 2a. The effective blockage for

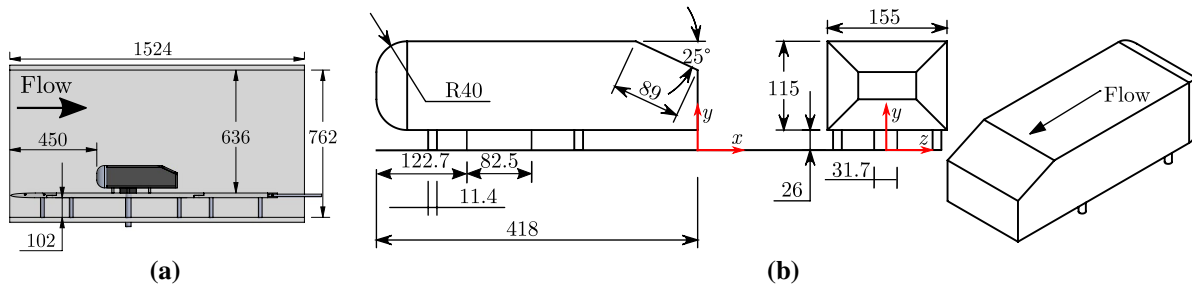


Fig. 2 Schematic of **a** test section with Ahmed body, **b** orthographic (side and front) and perspective views of Ahmed body. Dimensions are in millimeters (mm)

the working section (above the ground plane) is just below 3.6%. The free-stream velocity of the wind tunnel for all testing is $U_\infty = 40$ m/s, corresponding to a Reynolds number of $Re = 1.1 \times 10^6$, based on the length of the model, L .

2.2 Model details and test conditions

The Ahmed body with a slant angle of 25° is used as the reference model throughout the experiments. Dimensions of the 0.4 geometric scale Ahmed body used in the experiments are presented in Fig. 2b, including the height, $H = 115$ mm, and length, $L = 418$ mm. The model is supported on four standard cylindrical stilts close to the edges of the model and a support strut in the middle which is covered by a streamlined fairing carefully aligned with the flow to minimize disturbances. The coordinate system is also indicated, with the origin fixed on the floor of the ground plane at the intersection of the model symmetry plane and the rear vertical surface. The model is placed 450 mm from the front of the test section with a ground clearance of $C = 26$ mm. This clearance was chosen to ensure that the bulk of the Ahmed model is sufficiently above the boundary layer and in the free stream, so as to minimize ground effects due to the

boundary layer. The ground plane boundary layer measured 660 mm from the front of the test section (without model) was observed to be $\delta = 9.5$ mm.

2.3 Experimental techniques

The current study uses multiple velocity measurement techniques. stacked stereoscopic PIV and tomographic PIV are used to obtain volumetric information in the wake, while planar PIV is used to measure the in-plane flow components ($2D - 2C$) above the slant edge and in the wake along the centerline symmetry plane. Comparison of planar PIV results with those extracted from the volumetric data is performed to provide validation and greater confidence in the latter results.

2.3.1 Planar particle image velocimetry (planar PIV)

A Quantel Evergreen 532 nm, 200 mJ/pulse dual head laser mounted on top of the wind tunnel and sheet forming optics were used to generate a 1 mm-thick laser sheet. The sheet is located at the mid span of the model aligned with the streamwise direction, as shown in Fig. 3a. The wind

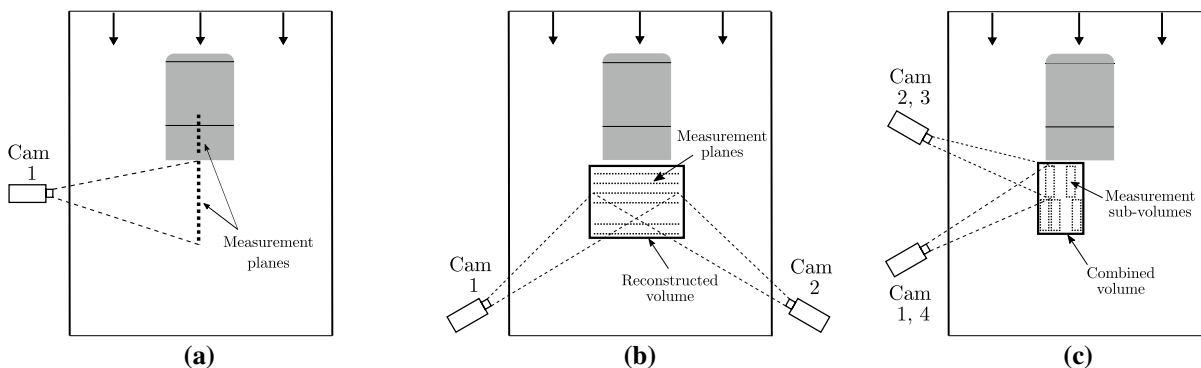


Fig. 3 Schematic of PIV setups. Top view of the $x - z$ plane showing cartoon of Ahmed model (gray shade) in test section with flow going from top to bottom and approximate orientation and location of cameras. **a** Planar PIV, **b** SSPIV, and **c** TPIV (cameras 1 and 2 are located

underneath cameras 4 and 3, respectively). Objects are not to scale and only a small subset of measurement planes and sub-volumes are shown in **b** and **c**, respectively

tunnel is seeded via a Roscoe Delta 3000 fog machine that produces micro-sized droplets of glycol-based fog fluid. The laser is synchronized to a double-frame camera (LaVision sCMOS) with 2560×2160 pixel resolution. Image pairs, with time separation of $10 \mu\text{s}$ between images, are acquired at 15 Hz with a total of 1200 image pairs captured to resolve the time-averaged statistics of the flow field. The images were processed using multiple passes in LaVision DaVis software, with two initial passes made with an interrogation window of 64×64 pixels and then a refined, third and fourth pass using a 32×32 pixel interrogation window. A 50% overlap was used for the initial passes, and a 75% overlap used on the final two passes, along with removal of spurious vectors. The resultant vector flow field has a 0.35×0.35 mm spatial resolution with a measurement uncertainty of $\sim 1.5\%$ calculated using correlation statistics (Wieneke 2015), with the highest uncertainties found in the regions of high shear. Additional information and comparison of various uncertainty quantification methods can be found in Sciacchitano et al. (2015).

2.3.2 Stacked stereoscopic particle image velocimetry (SSPIV)

The experimental setup for SSPIV measurements has two cameras mounted outside on either side of the test section and looking upstream into the rear vertical face of the Ahmed model, as shown in Fig. 3b. The flow was seeded and illuminated using the same setup as planar PIV, but the laser sheet was parallel to the rear vertical wall of the model and had a thickness of ~ 1.5 mm. Forty-five spanwise planes, covering the near wake region from 5 to 140 mm downstream of the rear vertical wall with streamwise spacing of 3 mm, were imaged at 15 Hz. Each spanwise plane had a width of 180 mm and height 145 mm centered about the Ahmed model centerline. Flow field images, with a resolution of 2560×2160 pixels, were acquired using two LaVision sCMOS cameras outfitted with Scheimpflug adapters to correct for the oblique view of the laser sheet by the cameras. Images were acquired, de-warped, and processed using LaVision DaVis software. Three-component velocity fields were calculated using a multi-pass, stereo-cross-correlation algorithm and had an in-plane spatial resolution of 0.8 mm with measurement uncertainties of $\sim 6\%$ within the regions of highest shear and $\sim 1.5\%$ in the rest of the near-wake region. At each measurement, plane 300 instantaneous velocity fields were acquired and time-averaged to obtain the mean velocity field. The $2D - 3C$ mean velocity fields acquired over all measurement planes were combined through linear interpolation to reconstruct the 3D velocity field over the entire volume.

2.3.3 Tomographic particle image velocimetry (TPIV)

Tomographic PIV allows for the direct measurement of instantaneous, three-dimensional velocity fields Scarano (2013), but is significantly more expensive in terms of hardware and computational requirements. Theoretical aspects of TPIV have been described in the existing literature (Elsinga et al. 2006; Scarano 2013) and only details specific to the current setup are discussed herein. In the present study, four LaVision sCMOS cameras equipped with Scheimpflug adapters, identical to the cameras used for SSPIV described above, were mounted on one side of the tunnel (see Fig. 3c). They were placed in a square configuration, such that they formed the vertices of a square, and were nominally equidistant from the measurement volume. Due to the relatively large extent of the wake region, and utilizing the inherent symmetry of the wake about the model centerline, only one half of the wake was studied. This region of interest was further divided into 18 sub-volumes and TPIV measurements were obtained in these sub-volumes and combined together.

A 400 mJ/pulse Quantel Evergreen double-pulsed laser and light volume forming optics were used to illuminate the measurement sub-volumes. The sub-volumes adjacent to the rear vertical surface of the model were located ~ 3 mm downstream from the wall to prevent direct light reflections saturating the image background of cameras 1 and 4. $f_{\#}$ for the camera lenses were set to 11 for the cameras in forward scattering and 8 for the cameras in backward scattering configurations. Calibration images for all cameras were acquired for every sub-volume using a precision machined two-level calibration plate (*LaVision Type 22*) and the mapping between image planes and physical space was calculated. As discussed in prior studies (Scarano and Poelma 2009; Scarano 2013), the requirement of relative positional accuracy between cameras is more stringent in TPIV compared to SSPIV. This was achieved through an *a posteriori* correction of the mapping function using the volume self-calibration procedure described by Wieneke (2008) and as implemented in LaVision DaVis 8.4.0 software. Through this procedure, the calibration errors were reduced to less than 0.05 pixels for all cameras, adequate for accurate tomographic reconstruction.

Two hundred and fifty double-frame images, with time separation of $10 \mu\text{s}$ between frames, were acquired at a frame rate of 10 Hz and processed using LaVision DaVis software. Convergence to the mean flow features was found to occur with approximately 120 image pairs, therefore, the mean results presented herein, calculated using a larger number of samples, are assumed to be fully converged. Tomographic volume reconstruction of the intensity distribution, using the MLOS and SMART (Atkinson and Soria 2009) algorithms with intermediate Gaussian volume smoothing (Discetti et al. 2013) and implemented in

LaVision DaVis as the fastMART algorithm, was performed using six iterations, yielding a reconstructed volume of size $60 \text{ mm} \times 85 \text{ mm} \times 10 \text{ mm}$ [streamwise (x), wall-normal (y), and spanwise (z) directions respectively], with z dimension being the light volume thickness, at $\sim 0.04 \text{ mm/voxel}$ resolution. Three-dimensional velocity vector fields were calculated by direct 3D cross correlation of the reconstructed volumes using a multi-pass algorithm with interrogation volumes of size $96 \times 96 \times 96$ voxels for the first pass and $44 \times 44 \times 44$ voxels with 75% overlap for the final pass, resulting in vector fields with spatial resolution of $\sim 0.5 \text{ mm}$. Spurious vectors were removed through a universal outlier detection method (Westerweel and Scarano 2005). Mean three-dimensional velocity fields from all sub-volumes were combined together and interpolated onto a regular volumetric grid $115 \text{ mm} \times 85 \text{ mm} \times 84 \text{ mm}$ encompassing one half of the symmetric wake region. While uncertainty in TPIV measurements is a topic of active research and different methods have been proposed (Kähler et al. 2016), an estimate of uncertainty in the time-averaged velocity is obtained based on the standard deviation of the velocity ensemble similar to the efforts outlined in Terra et al. (2017). The highest values of relative uncertainty in the mean statistics of velocity occurred in the wake shear layers and were found to be $\sim 4\%$, with significantly lower relative uncertainty outside of the shear layers.

3 Results and discussion

Models of the wake due to flow around the Ahmed body have been proposed (Vino et al. 2005; Ahmed et al. 1984) to have complex, three-dimensional flow topology, and planar (Thacker et al. 2013; Aubrun et al. 2011; Joseph et al. 2012), and stacked SPIV measurements (Venning et al. 2015) have offered proof of this, along with changes effected by control. While these studies offer a tantalizing preview of the complex flow topology, it is necessary to obtain volumetric information to fully capture the spatially varying nature of this wake. The present study provides a systematic analysis of the major flow features in the near wake, namely, trailing wake and streamwise vortices (shown schematically in Fig. 1). The comparative strengths and weaknesses of the two measurement techniques applied to this flow are also commented upon.

While the main focus of this study is on the near-wake flow structures, it is important to be aware of the flow over the slant surface which leads to the structures present in the near wake. Figure 4 shows planar PIV measurements of the normalized streamwise velocity, u/U_∞ , present above the slant surface along the symmetry plane. The superimposed streamlines clearly indicate flow separation close to the top of the slant and reattachment back on to the surface just

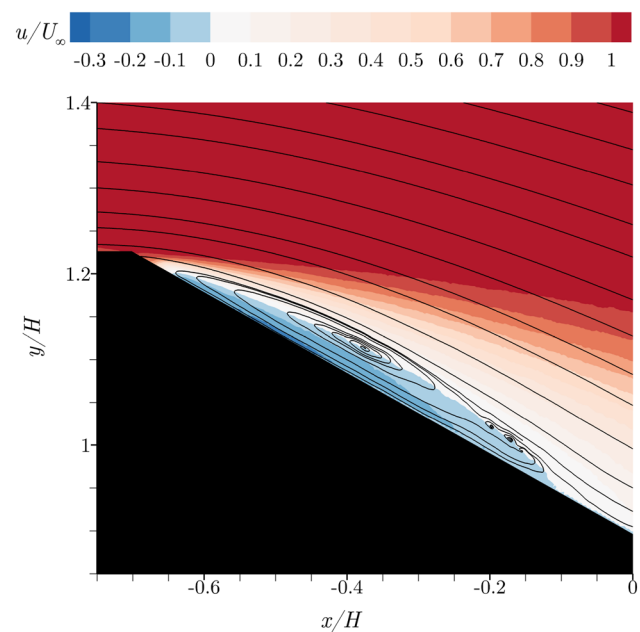


Fig. 4 Normalized streamwise velocity, u/U_∞ , above the slant surface at the model symmetry plane measured using planar PIV. Streamlines superimposed and flow is from left to right

upstream of the bottom edge of the slant. This flow pattern, with the separation bubble that is present, leads to the near-wake flow that is the focus of the present study.

3.1 Baseline flow topology

3.1.1 Wake vortices

To investigate the near wake of the model, spanwise planes were extracted from the volumetric measurements made through TPIV. Figure 5 shows the time-averaged, normalized streamwise velocity component, u/U_∞ , at spanwise locations ranging from $z/H = 0$ (centerline) to $z/H = 0.6$ (near the vertical side wall of model) and the streamwise extent ranging from just downstream of the rear wall of the model, $x/H = 0$, to $x/H = 1.0$. The blue colored contours indicate regions of reversed flow, and superimposed streamlines visualize the upper horseshoe vortex (*A*-vortex) and lower horseshoe vortex (*B*-vortex) in the wake. At the centerline symmetry plane ($z/H = 0$), similar to the planar PIV results from Tunay et al. (2014) and Zhang et al. (2015), the recirculation region extends up to $x/H = 0.65$ and the upper vortex is larger than the lower vortex and its vortical center is also closer to the rear surface of the model. Numerical results at $Re = 768,000$ (Minguez et al. 2008) show a similar arrangement of vortices with a more compact recirculation region, while Krajnović and Davidson (2005a) measured the recirculation length in the symmetry plane to be similar to the present study. The distance of the vortical center of the

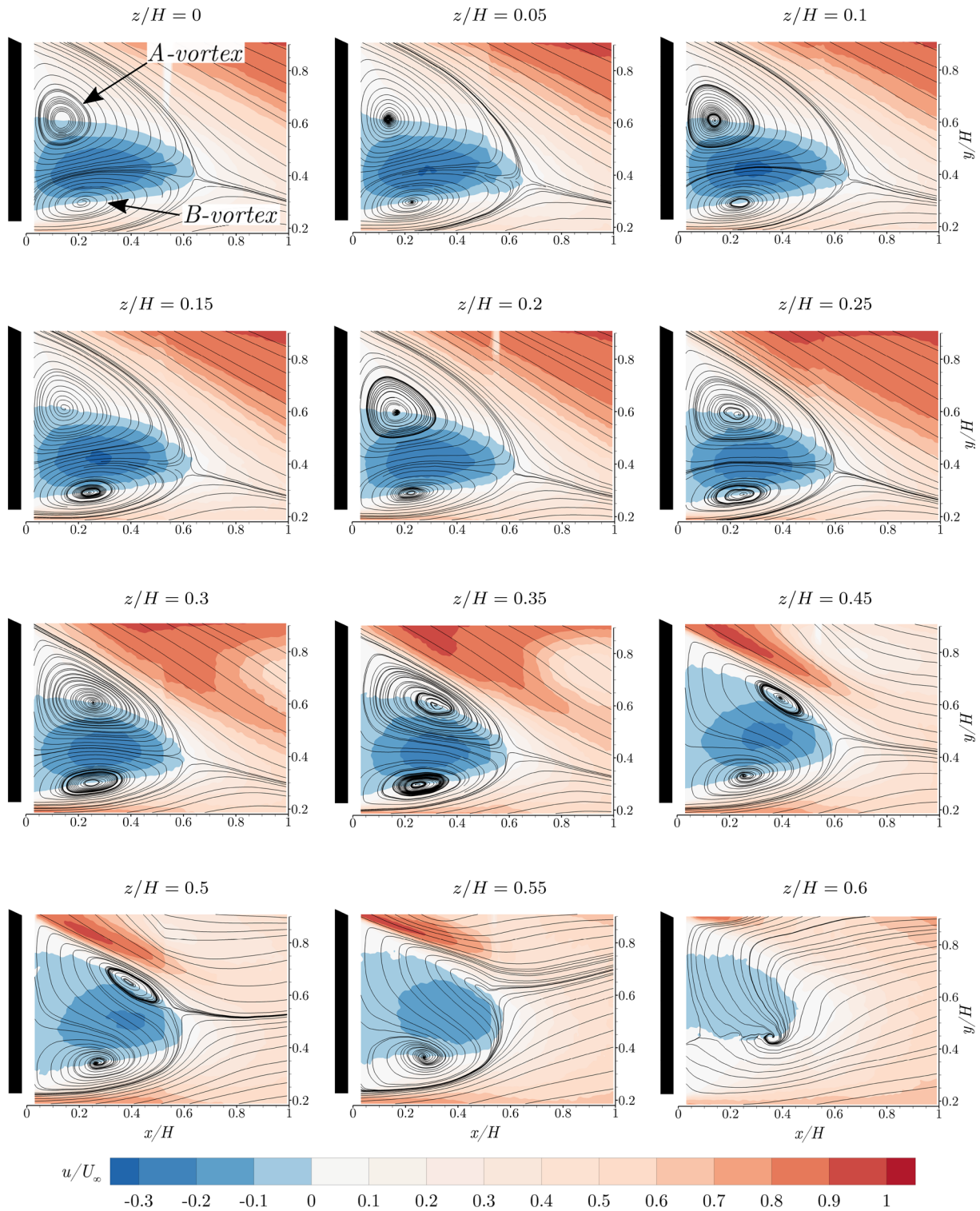


Fig. 5 Normalized streamwise velocity component, u/U_∞ , measured through TPIV, in the $x - y$ plane at various spanwise (z / H) locations. Streamlines superimposed. Flow is from left to right

A-vortex from the rear surface increases in spanwise planes away from the centerline. At $z/H = 0.25$, the centers of the upper and lower vortices are approximately equidistant from

the rear surface, with the upper vortex being larger. Moving further towards the edge of the model, the A-vortex becomes smaller, while its center moves further downstream and away

from the rear surface. At $z/H = 0.55$, it tapers off and disappears. The B -vortex persists further in the spanwise direction than the A -vortex, with a coherent vortical structure persisting until $z/H = 0.55$ and disappearing only by $z/H = 0.6$. The vortical center of the B -vortex (at $z/H \leq 0.55$) is found to be remarkably stable with increase in z/H and is located around $y/H = 0.3$ and $x/H = 0.2 - 0.3$. However, beyond $z/H = 0.55$, it abruptly tends upwards and slightly downstream to around $x/H = 0.4$ before merging and disappearing, possibly due to a complex three-dimensional interaction with the tail of the upper A -vortex and the flow coming around the side of the model that is affected by the C -pillar vortex.

The trajectory of the A -vortex described above is also observed in Figs. 6 and 7. Figure 6 shows the contours of time-averaged, normalized streamwise vorticity, $\omega_x H/U_\infty$, in the $y - z$ plane extracted from SSPIV measurements at various streamwise (x/H) locations, with blue contours indicating clockwise rotation and red contours indicating counter-clockwise rotation about the x axis when viewed upstream in a normal direction to the rear vertical surface. In-plane streamlines are also superimposed. The streamlines show the A -vortex appearing in the $x/H = 0.2$ plane and centered near $z/H = 0.25$ and $y/H = 0.6$. In subsequent x/H planes, this vortex moves outwards, along with the appearance of negative (clockwise) vorticity contours, consistent with the location and trajectory of the A -vortex. The vortex fully merges with the C -pillar by $x/H = 0.7$. Venning et al. (2017) accorded initial experimental support for this merging process, with the present results extending that support further by providing the exact location and topology of the vortical structures. In contrast, the trajectory of the B -vortex is oriented, such that there is no clear signature of its presence in the streamlines in the $y - z$ planes. Only a few patches of positive (counter-clockwise) vorticity contours appearing in the lower half of the planes around $x/H = 0.3 - 0.6$ mark the existence of the B -vortex.

Figure 7 shows orthographic views of the iso-surfaces of $u/U_\infty = 0$ in blue and Q-criterion (iso-level = 5), which is the second invariant of the velocity gradient tensor (Hunt et al. 1988), in red. Three-dimensional streamlines with seed points within the A - and B -vortices are also superimposed. The top view shows the streamlines with seed points within the A -vortex embedded within the $u/U_\infty = 0$ iso-surface, along with some of the streamlines of the B -vortex that are also visible at the right edge. The trajectory of the A -vortex, marked approximately by a manually drawn white, dashed line, can be discerned curving downstream. The A -vortex trajectory is similar to that observed at a lower Re in Venning et al. (2017). The back and side views show the complex path of the streamlines with seed points within the B -vortex. These streamlines are embedded along the bottom of the $u/U_\infty = 0$ iso-surface

from $z/H = 0$ to ~ 0.55 , with the approximate trajectory of the B -vortex indicated by manually drawn, *dash-dot* lines in Fig. 7c. Beyond that ($z/H > 0.55$) the streamlines, and implicitly the vortex itself, curves obliquely upwards and also in the streamwise direction, wrapping around the side of the iso-surface and thereby shaping the side of the iso-surface. Based on these observations, we can define both major wake vortices as horseshoe vortices. The A -vortex has a horizontal horseshoe shape with its legs pointing downstream, while the B -vortex is shaped similar to a nearly vertical horseshoe with legs angled obliquely downstream.

3.1.2 C-pillar vortices

The longitudinal C -pillar vortices observed on either side of the symmetry plane are known to originate on top of the slant and extend far into the wake (Ahmed et al. 1984; Vio et al. 2005; Krajnović and Davidson 2005b), as shown in Fig. 1. Figure 6 shows nine streamwise planes, ranging from $x/H = 0.1 - 0.9$; within those the evolution of the C -pillar is apparent. The C -pillar has a compact circular cross section close to the model, but quickly grows larger and less organized as it moves downstream. This is due to the interaction of the C -pillar vortex with the A - and B -vortices, which is also seen in the superimposed streamlines that help to elucidate the interplay between these structures. From $x/H = 0.2$ to $x/H = 0.4$, two distinct vortical regions are apparent in the streamlines, which indicate the initiation of the merging process between the C -pillar and A -vortex. Around $x/H = 0.5$, the core of the C -pillar is located between $z/H = 0.4 - 0.5$ and $y/H = 0.8 - 0.9$; this places it in close proximity to the upper horseshoe A -vortex, thereby playing a role in the distorted shape and eventual dissipation of the A -vortex. Further downstream, there is rapid loss in compactness of the C -pillar as it diffuses and takes on an asymmetric shape. The overall trajectory of the C -pillar is directed inwards towards the symmetry plane, as well as slightly downwards. This is readily apparent in the orthographic views shown in Fig. 7, where the iso-surface of Q-criterion (red) marks the C -pillar. All three views indicate the oblique trajectory of the C -pillar. A similar trajectory is observed in the numerical work of Krajnović and Davidson (2005b) and in the conceptual flow model proposed by Zhang et al. (2015) based on planar PIV measurements. The volumetric results presented herein validate and quantify the proposed trajectory. The back view in Fig. 7 also shows the interplay between the C -pillar and the trailing wake, with the edges of the $u/U_\infty = 0$ iso-surface and the B -vortex streamlines clearly trending upwards towards the C -pillar.

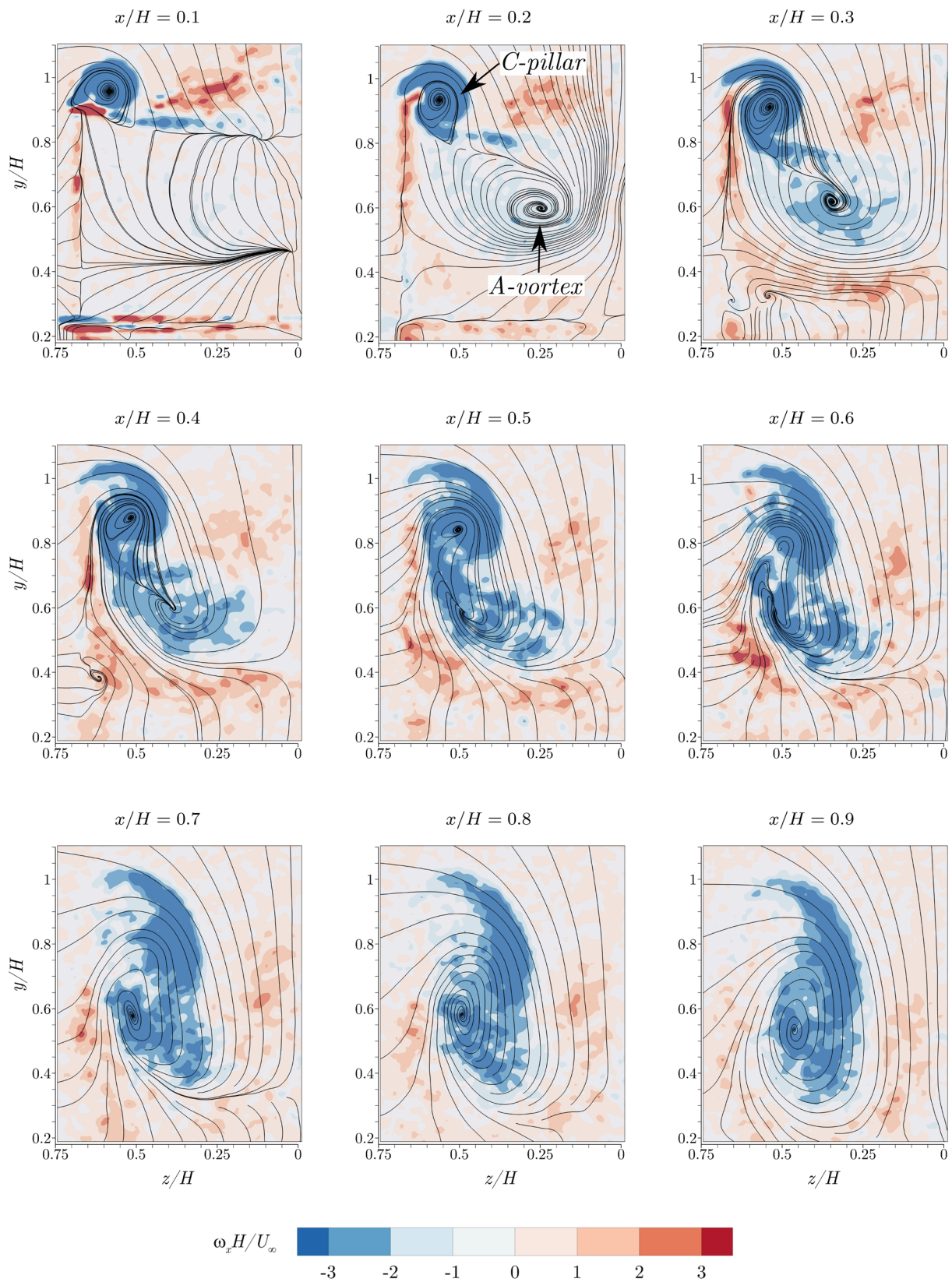


Fig. 6 Normalized streamwise vorticity, $\omega_x H / U_\infty$, measured through SSPIV, in flow normal ($y - z$) planes at various streamwise (x / H) locations. Streamlines superimposed. Flow is directed normally out of the surface

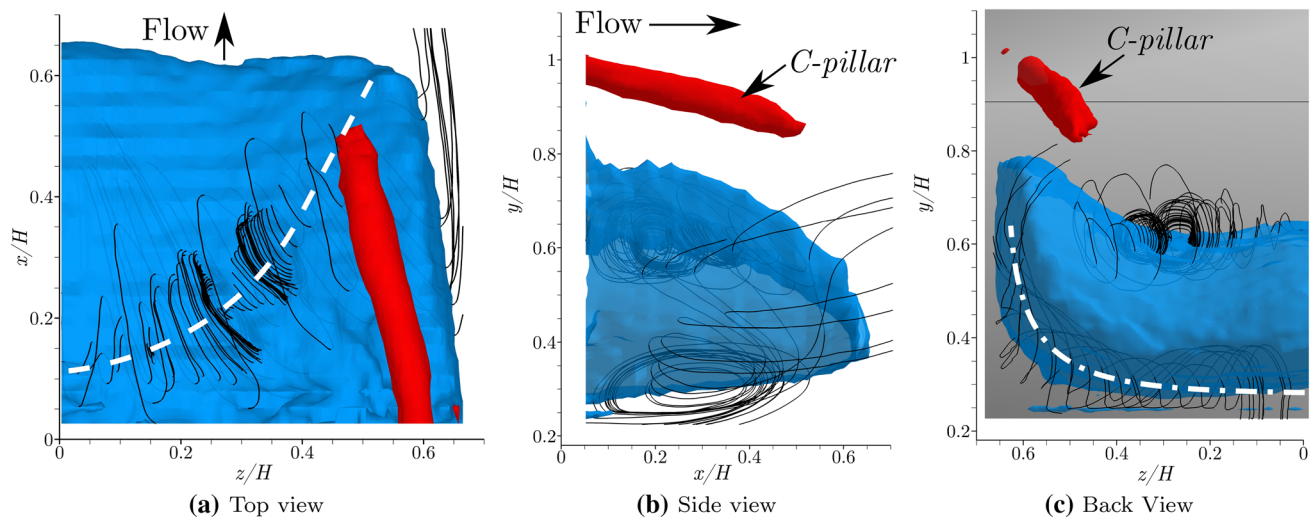


Fig. 7 Orthographic views of iso-surfaces of zero streamwise velocity ($u/U_\infty = 0$) encompassing reverse flow region shaded in translucent blue and Q-criterion (iso-level = 5) indicating C-pillar vortex shaded in red. Measured through SSPIV. Ahmed model shown in background in light gray shade. **a** Top view - white, dashed line indicates

approximate trajectory of A-vortex, **b** Side view, **c** Back view-flow is directed out normal to the surface and white dash-dot line indicates approximate trajectory of B-vortex. Solid, black lines indicate embedded three-dimensional streamlines with seed points within the A- and B-vortical structures

3.2 Flow topology and base pressure

Based on the above description of the three-dimensional topology, it is reasonable to hypothesize that the average pressure distribution on the rear surface should be correlated with the projection of the reversed flow region onto the rear surface (see back view shown in Fig. 7c). The pressure distribution on the rear surface affects pressure drag, and thereby the overall drag. Reversed flow towards the rear surface should lead to pressure recovery and relatively high pressure, while regions in close proximity to the vortical centers of the A and B vortices will exhibit a low-pressure signature. The region between the vortices has the largest magnitude of reversed flow and would have a corresponding high-pressure signature on the rear surface, with the effect most pronounced at the spanwise symmetry plane and tapering off towards the vertical outer edges of the rear surface. Close to the upper and lower edges of the rear surface along the symmetry plane, the presence of the A and B vortices leads to relatively lower pressures. The curved trajectory of the upper A-vortex sweeping outwards would lead to pressure recovery in the upper half of the rear surface away from the plane of symmetry and closer to the vertical side edges, but this might be tempered somewhat due to the presence of the C-pillar. Surface pressure distribution of low spatial resolution measured by McNally et al. (2015) at a slightly higher Re provide preliminary support for the pressure distribution proposed herein. Validation of this hypothesized pressure distribution, and any deviations from it, requires spatially

well-resolved surface pressure measurements and will be presented in a forthcoming paper.

The streamwise extent of the closed reverse flow region is also of interest as it indicates the length of the wake, which influences the base pressure and thereby affects the aerodynamic drag. Changes in the length of the wake with changing spanwise location are clearly seen in Fig. 7a through the top view of the iso-surface of $u/U_\infty = 0$ (blue) which encompasses the reverse flow region. At the symmetry plane ($z/H = 0$), the recirculation region extends up to $x/H \approx 0.65$, and decreases slightly to $x/H \approx 0.6$ by $z/H = 0.3$ before increasing again. Beyond $z/H = 0.6$, the zero velocity iso-surface falls steeply encompassing the closed reversed flow region.

3.3 Performance of SSPIV and TPIV

The flow topology described above was captured through two different volumetric methodologies, and as such, there were advantages and disadvantages to using either one. Whereas both measurement techniques provided similar information regarding the wake from a global perspective, the details and the cost were vastly different. Figure 8 shows the symmetry plane slices of normalized streamwise velocity (u/U_∞) extracted from data obtained through (a) planar PIV, (b) TPIV, and (c) SSPIV, for the baseline configuration. The SSPIV and planar PIV data have a larger vertical spatial extent than the TPIV data and are, therefore, able to capture a larger portion of the wake. Planar PIV uses a normal view, unaffected by stray reflections, of a relatively

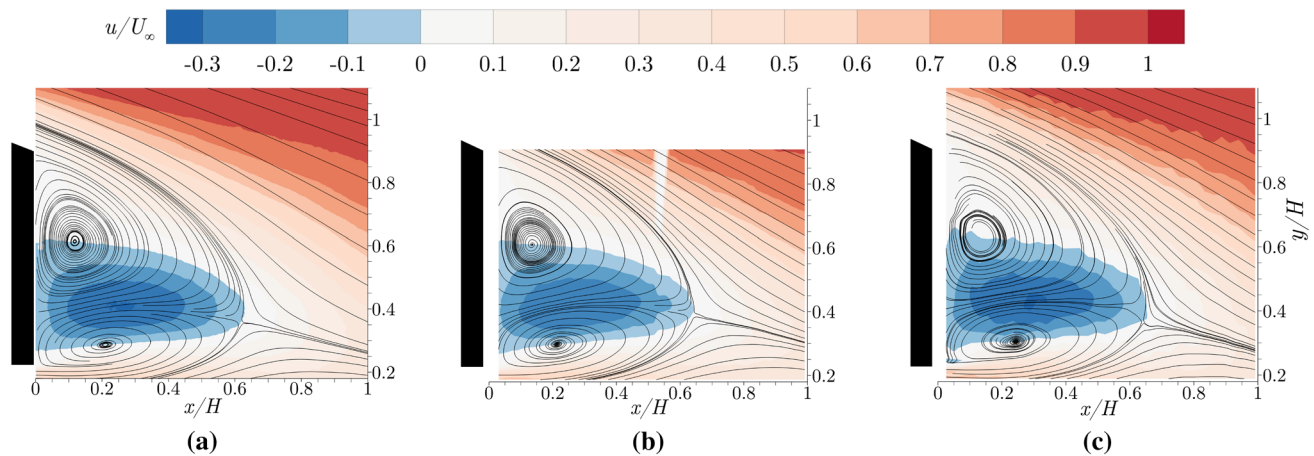


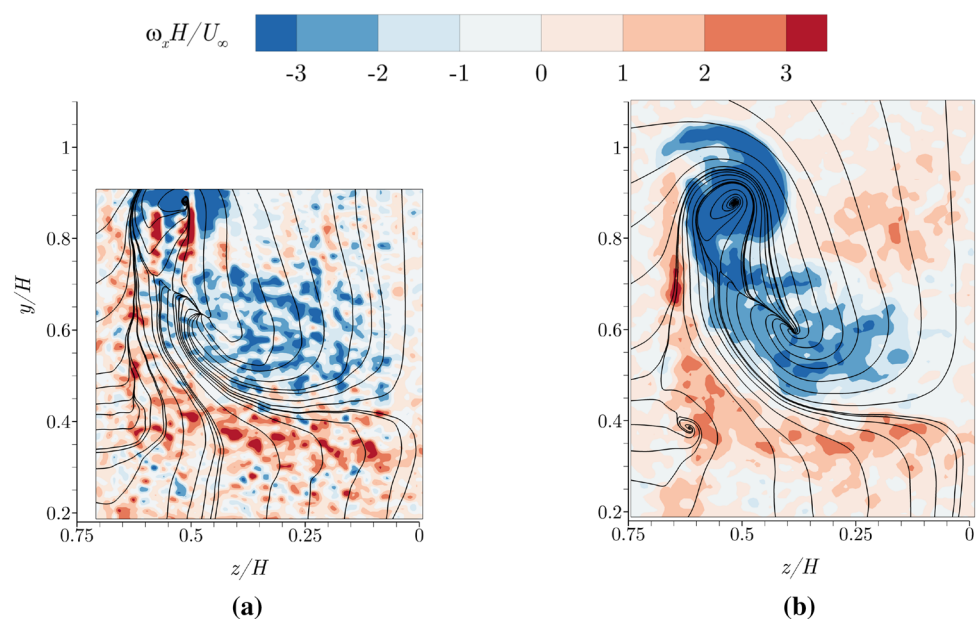
Fig. 8 Comparison of normalized streamwise velocity, u/U_∞ , along centerline ($z/H = 0$), in the $x - y$ plane. Velocity fields obtained through **a** Planar PIV, **b** TPIV, and **c** SSPIV. Streamlines superimposed, model shown shaded in black, and flow is from left to right

thin light sheet and therefore measurements close to the rear wall of the model are possible. Both TPIV and SSPIV involve oblique camera views that suffer from background reflections when the rear vertical wall is illuminated. This necessitates careful alignment of the light sheet/volume to avoid illuminating the rear vertical surface of the model, thereby precluding any measurements closer than ~ 3 mm to the model (see Fig. 8b, c). Streamlines superimposed on the contours indicate the upper A and lower B vortices, and it is apparent that both volumetric methods reliably capture the large-scale vortex structures and are qualitatively comparable to the more accurate planar PIV measurements. However, a closer examination of the contours in the SSPIV data reveals a rough, jagged appearance. This is because the original measurements were acquired in discrete $2D$ planes

normal to the centerline plane (see Fig. 3b) shown and the spacing between planes is larger than the spatial resolution of TPIV, thereby resulting in a lower spatial resolution than the TPIV measurements in the $x - y$ plane. The TPIV data have smoother contours, but it does suffer from an artifact, where the measurement sub-volumes were merged together (at $x/H \approx 0.5$).

The situation is reversed when extracting streamwise slices from the volumetric data, as shown in Fig. 9. The flow normal planes in Fig. 9 show contours of normalized streamwise vorticity extracted from TPIV and SSPIV data at $x/H = 0.4$. While the TPIV data capture a portion of the downstream section of the C -pillar vortex core, the overall vortex structure is not as well resolved and smooth as in the SSPIV data and suffers from minor artifacts, but regions

Fig. 9 Normalized vorticity component, $\omega_x H/U_\infty$, in flow normal ($y - z$) plane located at $x/H = 0.4$. Streamlines superimposed. Measurements obtained through **a** TPIV, and **b** SSPIV



of positive (red) and negative (blue) vorticity measured by the two techniques appear equivalent. Streamlines superimposed on the contours indicate the location of the vortex core and the bifurcation region, and both TPIV and SSPIV techniques reliably capture these flow features. The SSPIV data look qualitatively better and less noisy than the TPIV data in the $y-z$ plane due to its ability to obtain robust in-plane measurements even in less-than-ideal conditions. Its larger spatial extent in the vertical direction also allows for capturing the C -pillar vortex closer to the rear vertical surface ($x/H = 0$). The compact C -pillar vortex core also has a lower particle concentration, with only smaller (lighter) particles penetrating the core, which leads to a less accurate and more noisy measurement through TPIV, since it is more sensitive to particle seeding density.

These qualitative assessments are buttressed by quantitative comparisons of velocity profiles extracted from the volumetric data with those measured through planar PIV. Figure 10 shows the longitudinal velocity profiles extracted at multiple streamwise locations ($x/H = 0.25, 0.50, 0.75, 0.95$) along the symmetry plane. It is readily apparent that the overall trends are similar between the three techniques. The TPIV velocity profiles track the planar PIV results closely, while the SSPIV technique gives slightly lower values for the velocities. This underestimation can be caused due to the lower spatial resolution of SSPIV in the flow direction, and since the data for the three measurement techniques were obtained during chronologically separated testing

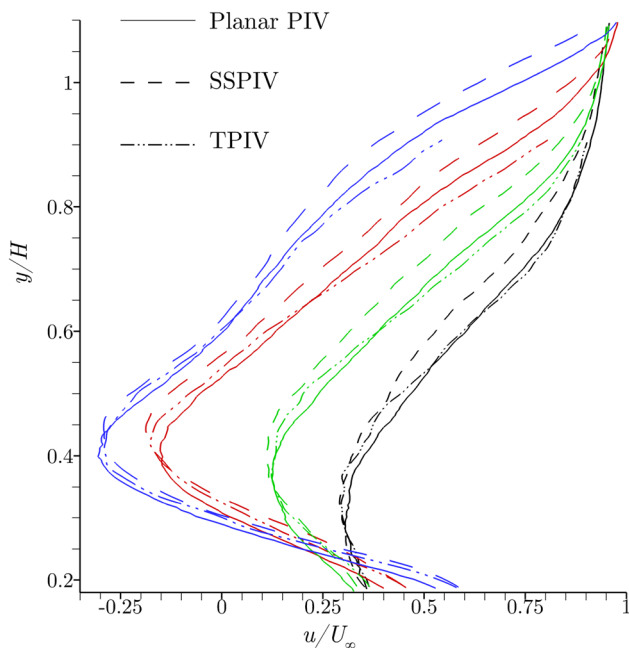


Fig. 10 Longitudinal velocity profiles along the symmetry plane extracted at $x/H = 0.25$ (blue), 0.50 (red), 0.75 (green), and 0.95 (black)

campaigns, due to minor variability in the tunnel free-stream flow conditions between campaigns. This close agreement with planar PIV results, obtained from averaging 1200 vector fields, also provides assurance of convergence of mean statistics obtained through SSPIV and TPIV. The velocity profiles extracted from TPIV data at $x/H = 0.25$ (blue) and $x/H = 0.50$ (red) diverge slightly from the planar PIV results around $y/H = 0.80$ due to the shear layer present at those locations, whereas the other two TPIV velocity profiles closely track with the planar PIV results due to the lack of shear, thereby exemplifying the decrease of TPIV accuracy in the presence of a steep velocity gradient.

The computational cost of TPIV was found to be much higher than SSPIV. While the specific computational cost of TPIV depends on a number of parameters such as the quality of volumetric reconstruction, size of measurement volume, and the vector spatial resolution, even the most conservative choices in these parameters lead to higher overall computational cost compared to SSPIV. The overall computational cost of the stacked SPIV technique is mainly dependent on the desired spatial resolution in the direction normal to the measurement planes. Achieving a higher spatial resolution would require increasing the number of measurement planes and will lead to an increased computational cost for the same overall measurement volume.

While not relevant to the present study which only looked at time-averaged quantities, characterizing the instantaneous three-dimensional flow topology is not possible with the stacked SPIV technique. Since TPIV is capable of providing truly volumetric measurements if sufficient illumination coupled with appropriate particle seeding concentration is available, it is possible to measure larger volumes than was attempted in the present study that would allow for the characterization of instantaneous three-dimensional flow fields and the associated dynamics of such a flow field.

4 Conclusion

The present study describes the complex, three-dimensional topology of the flow field in the wake of a 25° Ahmed model. While the salient features of this flow field have been described before, their variation in three-dimensional space was explored herein. The trailing wake vortices were found to vary in size and shape along the spanwise direction, with the A - and B vortices undergoing a complex interaction with the C -pillar vortex. Both vortices are nominally horseshoe shaped, with the upper A -vortex core located closer than the core of the B -vortex to the rear surface at the model symmetry plane. Away from the symmetry plane, the A -vortex rapidly curves away from the rear surface and is oriented almost horizontally pointing downstream. The B -vortex stays parallel to the rear surface and spans almost to the edge of the

model before curving upwards to form a obliquely aligned horseshoe shape. The *C*-pillar vortex core was found to be small and compact close to the rear surface, but grows larger and dissipates moving downstream. The trajectory of the *C*-pillar is directed obliquely towards the symmetry plane.

The performance of the two measurement techniques, namely, stacked stereoscopic PIV and tomographic PIV, used in the study, was also analyzed, and quantitative comparisons with planar PIV were made. Both techniques were found to accurately capture volumetric information regarding the flow topology, albeit with certain inherent advantages and disadvantages in each case. Therefore, the most appropriate technique for future studies should be chosen taking into consideration the desired spatial resolution, available hardware and computational resources, and whether time-averaged or instantaneous quantities are of interest.

Acknowledgements The authors would like to thank Jeremy Phillips, Adam Piotrowski, and Bobby Avant for their help with model fabrication. The research is supported in part by the National Science Foundation PIRE program and the Florida Center for Advanced Aero-Propulsion (FCAAP).

References

- Ahmed S, Ramm G, Faltin G (1984) Some salient features of the time-averaged ground vehicle wake. *SAE Change* 2012:11–12
- Atkinson C, Soria J (2009) An efficient simultaneous reconstruction technique for tomographic particle image velocimetry. *Exp Fluids* 47(4–5):553
- Aubrun S, McNally J, Alvi F, Kourta A (2011) Separation flow control on a generic ground vehicle using steady microjet arrays. *Exp Fluids* 51(5):1177–1187
- Bruneau CH, Mortazavi I, Gilliéron P (2008) Passive control around the two-dimensional square back ahmed body using porous devices. *J Fluids Eng* 130(6):061101
- Conan B, Anthoine J, Planquart P (2011) Experimental aerodynamic study of a car-type bluff body. *Exp Fluids* 50(5):1273–1284
- Corallo M, Sheridan J, Thompson M (2015) Effect of aspect ratio on the near-wake flow structure of an ahmed body. *J Wind Eng Ind Aerodyn* 147:95–103
- Discetti S, Natale A, Astarita T (2013) Spatial filtering improved tomographic PIV. *Exp Fluids* 54(4):1505
- Elsinga GE, Scarano F, Wieneke B, van Oudheusden BW (2006) Tomographic particle image velocimetry. *Exp Fluids* 41(6):933–947
- Fares E (2006) Unsteady flow simulation of the ahmed reference body using a lattice boltzmann approach. *Comput Fluids* 35(8–9):940–950
- Froling T, Juechter T (2005) 2006 chevrolet corvette C6 Z06 aerodynamic development. Tech. rep., SAE Technical Paper
- Hunt JC, Wray AA, Moin P (1988) Eddies, streams, and convergence zones in turbulent flows. Center for Turbulence Research Report CTR-S88, pp 193–208
- Joseph P, Amandolèse X, Aider JL (2012) Drag reduction on the 25 slant angle ahmed reference body using pulsed jets. *Exp Fluids* 52(5):1169–1185
- Joseph P, Amandolèse X, Edouard C, Aider JL (2013) Flow control using mems pulsed micro-jets on the ahmed body. *Exp Fluids* 54(1):1–12
- Kähler CJ, Astarita T, Vlachos PP, Sakakibara J, Hain R, Discetti S, La Foy R, Cierpka C (2016) Main results of the 4th International PIV challenge. *Exp Fluids* 57(6):97
- Kourta A, Gillieron P (2009) Impact of the automotive aerodynamic control on the economic issues. *J Appl Fluid Mech* 2(2):69–75
- Krajnović S, Davidson L (2005a) Flow around a simplified car, part 1: large eddy simulation. *J Fluids Eng* 127(5):907–918
- Krajnović S, Davidson L (2005b) Flow around a simplified car, part 2: understanding the flow. *J Fluids Eng* 127(5):919–928
- Lienhart H, Becker S (2003) Flow and turbulence structure in the wake of a simplified car model. SAE Technical Paper, SAE International. <https://doi.org/10.4271/2003-01-0656>
- Lienhart H, Stoots C, Becker S (2002) Flow and turbulence structures in the wake of a simplified car model (Ahmed modell). In: Wagner S, Rist U, Heinemann H-J, Hilbig R (eds) New results in numerical and experimental fluid mechanics III. Springer, Berlin, Heidelberg, pp 323–330. https://doi.org/10.1007/978-3-540-45466-3_39
- McNally J, Fernandez E, Kumar R, Alvi F (2012) Near wake dynamics for an Ahmed body with active flow control. In: 6th AIAA flow control conference
- McNally JW, Alvi FS, Mazellier N, Kourta A (2015) Active flow control on an Ahmed body—an experimental study. In: 53rd AIAA aerospace sciences meeting, p 0825
- Metka M, Gregory JW (2015) Drag reduction on the 25-deg Ahmed model using fluidic oscillators. *J Fluids Eng* 137(5):051108
- Mínguez M, Pasquetti R, Serre E (2008) High-order large-eddy simulation of flow over the Ahmed body car model. *Phys Fluids* 20(9):095101
- Park H, Cho JH, Lee J, Lee DH, Kim KH (2013) Experimental study on synthetic jet array for aerodynamic drag reduction of a simplified car. *J Mech Sci Technol* 27(12):3721–3731
- Pujals G, Depardon S, Cossu C (2010) Drag reduction of a 3D bluff body using coherent streamwise streaks. *Exp Fluids* 49(5):1085–1094
- Rossitto G, Sicot C, Ferrand V, Borée J, Harambat F (2016) Influence of afterbody rounding on the pressure distribution over a fastback vehicle. *Exp Fluids* 57(3):43
- Scarano F (2013) Tomographic PIV: principles and practice. *Meas Sci Technol* 24(1):012001
- Scarano F, Poelma C (2009) Three-dimensional vorticity patterns of cylinder wakes. *Exp Fluids* 47(1):69
- Sciacchitano A, Neal DR, Smith BL, Warner SO, Vlachos PP, Wieneke B, Scarano F (2015) Collaborative framework for PIV uncertainty quantification: comparative assessment of methods. *Meas Sci Technol* 26(7):074004
- Terra W, Sciacchitano A, Scarano F (2017) Aerodynamic drag of a transiting sphere by large-scale tomographic-PIV. *Exp Fluids* 58(7):83
- Thacker A, Aubrun S, Leroy A, Devinant P (2012) Effects of suppressing the 3d separation on the rear slant on the flow structures around an Ahmed body. *J Wind Eng Ind Aerodyn* 107:237–243
- Thacker A, Aubrun S, Leroy A, Devinant P (2013) Experimental characterization of flow unsteadiness in the centerline plane of an Ahmed body rear slant. *Exp Fluids* 54(3):1–16
- Tunay T, Sahin B, Ozbolat V (2014) Effects of rear slant angles on the flow characteristics of Ahmed body. *Exp Thermal Fluid Sci* 57:165–176
- Venning J, Jacono DL, Burton D, Thompson M, Sheridan J (2015) The effect of aspect ratio on the wake of the ahmed body. *Exp Fluids* 56(6):126
- Venning J, Lo Jacono D, Burton D, Thompson MC, Sheridan J (2017) The nature of the vortical structures in the near wake of the ahmed body. *Proc Inst Mech Eng Part D J Automob Eng* 231(9):1239–1244. <https://doi.org/10.1177/0954407017690683>

- Vino G, Watkins S, Mousley P, Watmuff J, Prasad S (2005) Turbulent near wake of an Ahmed vehicle model. *J Fluids Struct* 20(5):673–695
- Wang X, Zhou Y, Pin Y, Chan T (2013) Turbulent near wake of an Ahmed vehicle model. *Exp Fluids* 54(4):1–19
- Westerweel J, Scarano F (2005) Universal outlier detection for PIV data. *Exp Fluids* 39(6):1096–1100
- Wieneke B (2008) Volume self-calibration for 3D particle image velocimetry. *Exp Fluids* 45(4):549–556
- Wieneke B (2015) Piv uncertainty quantification from correlation statistics. *Meas Sci Technol* 26(7):074002
- Zhang B, Zhou Y, To S (2015) Unsteady flow structures around a high-drag ahmed body. *J Fluid Mech* 777:291–326

Publisher's Note Springer Nature remains neutral with regard to jurisdictional claims in published maps and institutional affiliations.